Synthesis and Characterization of BFO Doped with Nickel

Dr Jyotsna Chauhan*, Poonam Patel

*HOD Department of Nanotechnology, Rajiv Ganhi Techanical University, Bhopal (M.P.), India
*Corresponding authors E-mail- jyotsnachauhan2006@gmail.com

Abstract: phase transformations at different compositions and develop different synthesis methods that can curb the formation of impurity phases. Chemical route can be used to synthesize nanocrystalline undoped and Ni-doped bismuth ferrite with perovskite structure and crystallite size of about 14nm and 15.4 nm, respectively. Rise in doping concentration leads to generation of secondary phase, thus dopant concentration is maintained to 5mol%. Morphological analyses exhibits irregular polygonal to bimodal shape agglomerates with few interconnected pores. Dielectric constant for the undoped bismuth ferrite is about 100, while for 5mol% Ni doped sample it is noted around 600 (at low frequency). Such drastic change leads to higher polarizability which also enhances ferroelectricity with Ni doping on perovskite bismuth ferrite. Both nanocrystalline and Ni-doped BFO exhibits super paramagnetic nature due to suppression of spin cycloid magcycloid magnetic moment. Saturation magnetization of Ni-doped is slightly lower than for undoped BFO due to smaller crystallite size.
[Jyotsna Chauhan, Poonam Patel. **Synthesis and Characterization of BFO Doped with Nickel.** *Rep Opinion* 2018;10(5):41-53]. ISSN 1553-9873 (print); ISSN 2375-7205 (online). http://www.sciencepub.net/report. 6. doi:10.7537/marsroj100518.06.

Keywords: ferroelectricity, XRD, FTIR

Introduction:.

Applications of BFO include new magnetic memory devices, smart sensors and spintronics technologies. Integrating the BFO into the silicon substrate as a single crystal makes the BFO more efficient by limiting the amount of electric charge that "leaks" out of the BFO into the substrate. It means by controlling the leakage current we can now developed smart devices that can sense, manipulate and respond to data more quickly because it all happens on one chip – the data doesn't need to be relayed elsewhere.

The simultaneous coexistence of at least two ferroic properties, (anti) ferromagnetism, (anti) ferroelectricity and (anti) ferroelasticity in the same phase is defined as multiferroics, as shown in Figure 1.2. These materials have the potential of exhibiting coupling between and magnetism, known as the magnetoelectric effect, which enables the external electric field to change magnetization and vice versa.

Bismuth ferrite (BiFeO3), is an inorganic chemical compound with a perovskite structure and an unusual compound of bismuth, iron, and oxygen (BFO). It is one of the most promising lead-free piezoelectric materials, which exhibits multiferroic properties at room temperature. Multiferroic materials exhibit ferroelectric or anti-ferroelectric properties in combination with ferromagnetic (or antiferromagnetic) properties in the same phase. As a result, an electric field can induce change in magnetization and an external magnetic field can induce electric polarization. This phenomenon is known as the magneto electric effect (ME) effect and materials exhibiting this effect are called magneto electrics or seignetto-magnets. Further proof of it being ferromagnetic is that it produces a hysteresis loop during ferroelectric characterization. The ability to couple to either the electric or the magnetic polarisation allows an additional degree of freedom in device designs. [10]

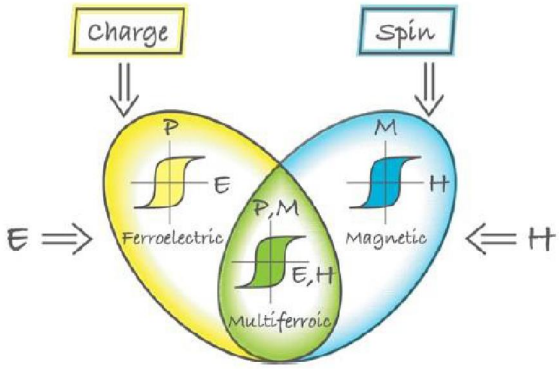

Figure 1.2 Schematic illustration of multiferroic defined from the overlap region of ferroelectric and magnetic

The lattice parameter and crystal structure of BiFeO3 are dependent on the temperature. The atomic coordination are slight changed between 5K and 300K. Significant changes are observed above 300K, the influence of temperature on the cell parameter, volume, bond distance and bond angle are shown below in Figure 1.8.

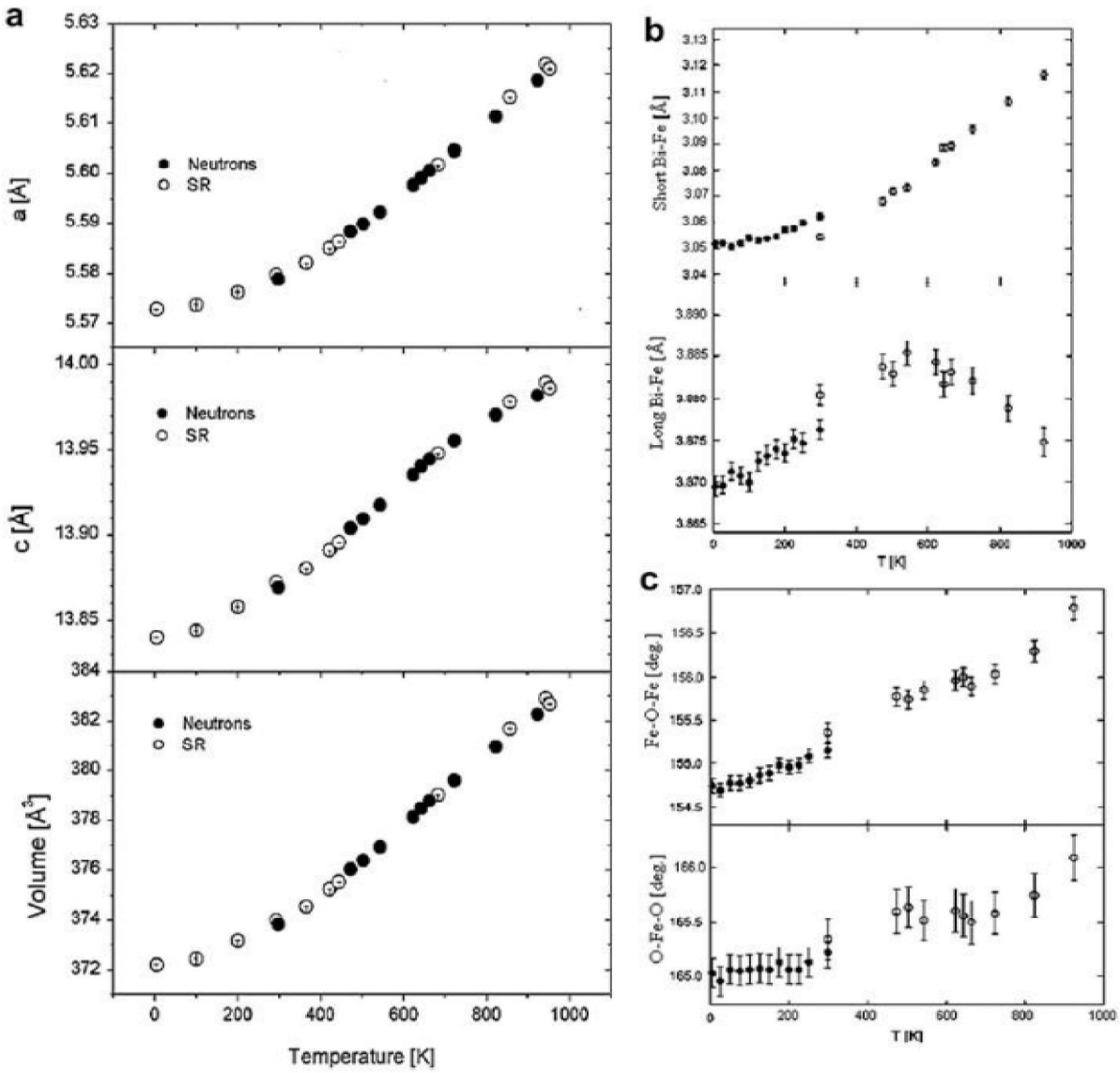

Figure 1.8Plots of temperature (0-1000K) as functions of (a) lattice parameter a, c and volume of BiFeO3(b) short and long distance of Bi-Fe bond (c) Fe-O-Fe and O-Fe-O angles. [18]

It was well documented that, except for the long Bi-Fe bond distance, the lattice parameter a, c, the volume of unit cell, the short bond distance of Bi-Fe as well as the bond angles gradually increase with increase in temperature. As a consequence of these variations, magnetism and polarization are reported to be gradually reduced, and structural phase transitions are also induced from the rhombohedrally distorted R3c perovskite structure to an orthorhombic P nma structure at 1098K and eventually to a cubic structure above 1204K. [19]

However, single phase BiFeO3 is difficult to synthesize. Due to the metastable nature of bismuth ferrite in air [20] as well as the volatility of bismuth oxide, their stoichiometry can be changed resulting in impurities of Bi2O3, Bi25FeO39 and Bi2FeO9 during the sintering process. The phase diagram of Fe2O3 and Bi2O3 is presented below in Figure 1.9 [20], unequal amount of Fe2O3 and Bi2O3 is seen to bring about impurity phases Bi25FeO39(bismuth-rich) and Bi2FeO9(bismuth-deficient).

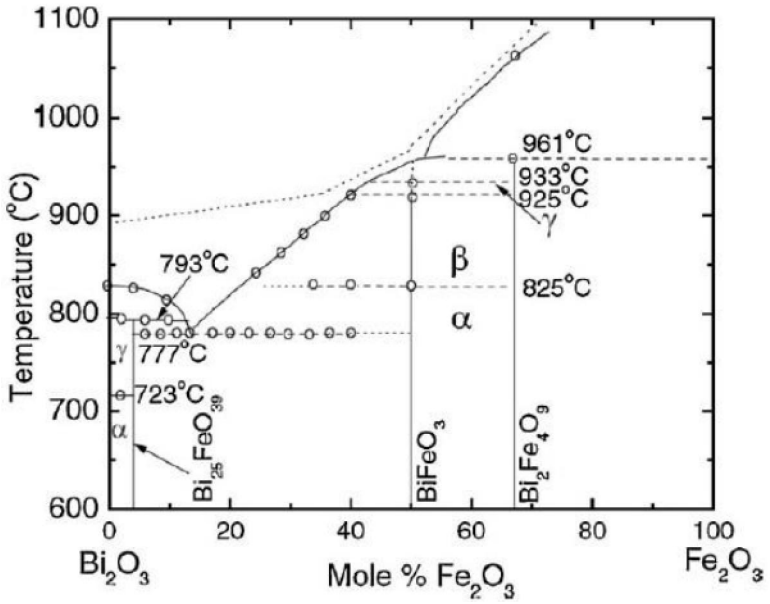

Figure 1.9 Phase diagram of Fe2O3and Bi2O3showing bismuth ferrite with undesired impurities. [12]

Experimental: Many techniques have been utilized to prepare BiFeO3 nanostructures. All of the reagents were of LR grade and used without further purification. Following a typical procedure, of bismuth nitrate [Bi (NO3)3·5H2O] and iron nitrate [Fe (NO3)3·9H2O] were weighed in stoichiometric proportions and dissolved in deionized water to make a solution with an independent concentration of 0.1M before adding 20mL diluted nitric acid (65∼68%HNO3) to the mixture. The light-yellow-colored solution was heated under vigorous stirring until no liquid was left in the beaker to form gel deposit. Each beaker with solid deposit was kept in the oven at 150◦C for another 2 -3h. Subsequently, powders were quarterly divided and calcined in the oven for 10-12 h at 550◦C, respectively, to obtain well-crystallized BFO NPs with controllable sizes.

For comparison, another group of powders were synthesized by modifying a typical soft chemical route by using excess tartaric acid as chelating agents [27].

The gel (intermediate product) was subjected to thermal analysis in order to determine the subsequent sintering temperature with simultaneous Moffel furnace. After heat treatment, the sample was characterized using X-ray diffraction. Fourier transformation infrared (FT-IR) spectra were obtained.

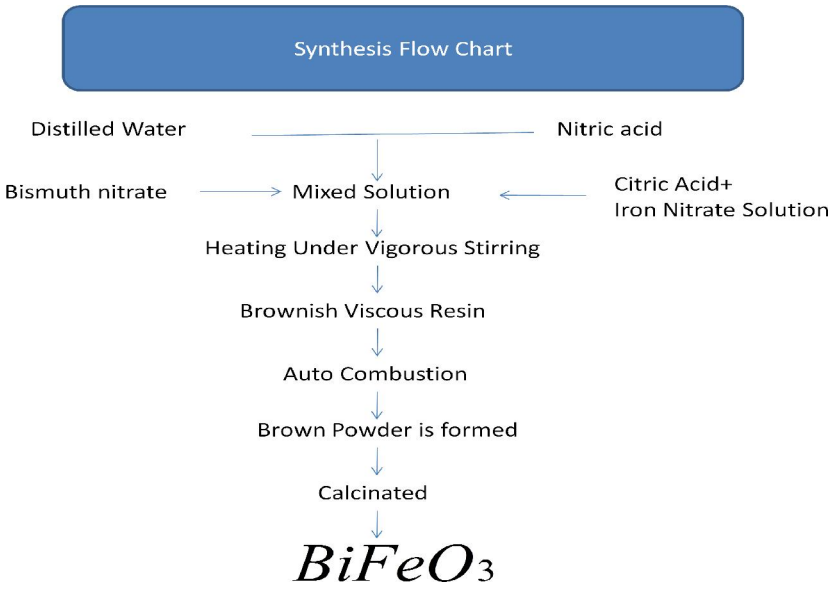

Figure 2.5 Diagram of pure BFO during stirring

Figure 2.5 is the picture of sample when we add the bimuth nitrate in the solution of DI water and nitric acid afterthis the sample is stirred being the colour of the should be transparent it means the process of prepration of the sample is true. If the colour of the sample is transparent.

Figure 2.6 Diagram of pure BFO during stirring after adding citric acid

Figure 2.6 is the picture of sample when we add both the solution with each other means colour of the sample is light yellow but after adding citric acid to the solution the colour of the sample is brown in colour this sample is stirred 12 to 15 hr for homogeneous solution after this sample is hgeated at 150℃ for 3-4 hr to calcinated the sample.

Flow Chart Of Synthesis Routes For Nickel Doped BFO:

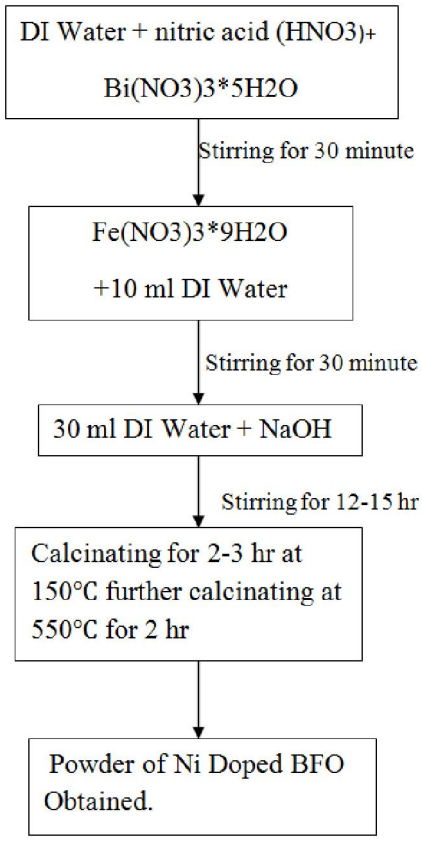

2.17 Experimental effect of Nickel Doped BFO:

BFO and Ni-doped BFO of BiFe1-*x*Ni*x*O3 were prepared by chemical route using precursor materials like bismuth nitrate [Bi (NO3)3×5H2O], ferric nitrate [Fe (NO3)3×9H2O], nickel nitrate and nitric acid. The solution was made of bismuth nitrate and ferric nitrate in 1:1 stoichiometric molar ratio, dissolved in the nitric acid and DI water. Each precursor was dissolved in the respective solvent to form a solution under constant stirring for 30 minutes. After ensuring that there is no sedimentation/precipitation, both precursors were mixed together and kept constant stirring for 12-15hr to homogenize mixing. The solution was subsequently heated to 150 °C for drying till (2–2.5 h) all liquids gets evaporated. The calcined sample was then quickly raised to proper thermal treatment temperatures of 550°C for 10-12 hour. The samples were leached using NaOH (20–30 drops) to remove impure phases and to balance the effect of nitric acid and obtain the phase pure undoped BFO and nickel doped BFO material.

The pelletized samples were then sintered at the same conditions used for heat treatment of the as-synthesized powder samples.

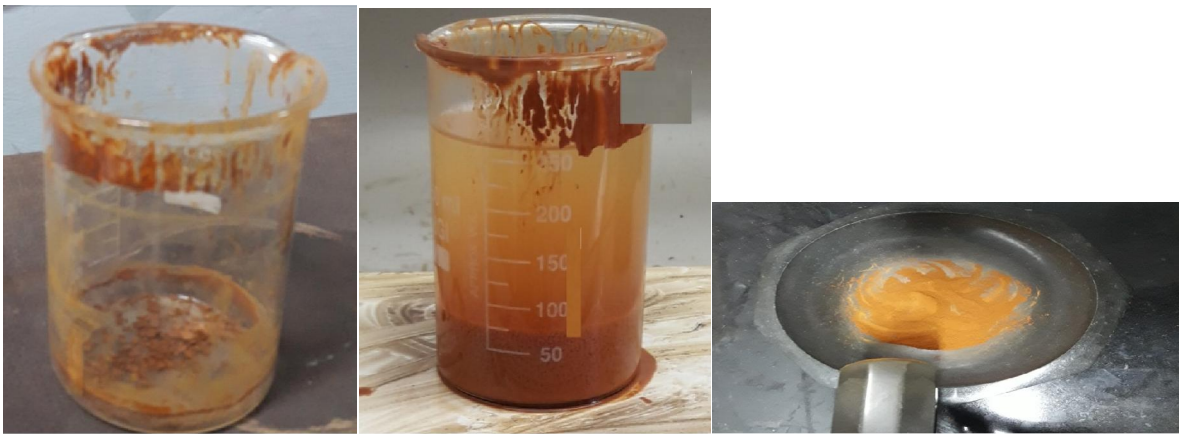

Figure 2.8 picture of Ni Doped sample at various condition

Results and discussion: FTIR RESULT OF PURE **BFO**

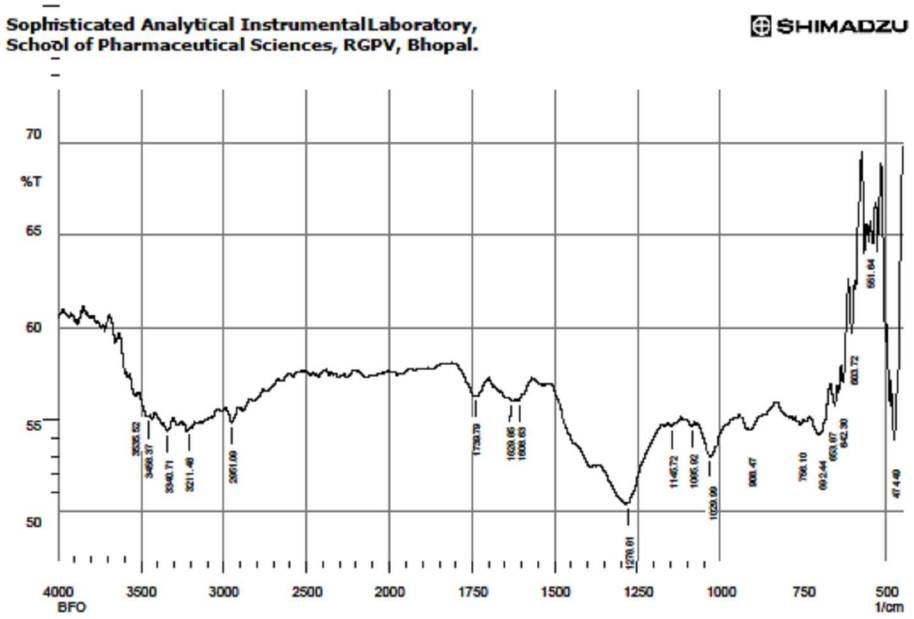

No.	Peak	Intensity	Corr. Intensity	Base (H)	Base (L)	Area	Corr. Area
1	474.49	53.86	6.79	484.13	449.41	8.07	1.14
2	551.64	64.67	0.83	555.5	547.78	1.44	0.02
3	603.72	59.68	2.92	613.36	594.08	4.1	0.18
4	642.3	56.45	0.72	646.15	634.58	2.82	0.02
5	653.87	55.73	1.11	667.37	646.15	5.29	0.09
6	692.44	54.3	0.19	694.37	667.37	6.9	0.04
7	756.1	54.72	0.23	763.81	748.38	4.03	0.02
8	908.47	54.42	0.17	912.33	889.18	6.07	0.03
9	1029.99	52.96	1.95	1068.56	958.62	29.35	0.76
10	1085.92	54.65	0.27	1103.28	1078.21	6.55	0.03
11	1145.72	54.6	0.31	1159.22	1118.71	10.58	0.05
12	1278.81	50.44	0.18	1282.66	1178.51	28.98	0.05
13	1608.63	56.03	0.15	1612.49	1570.06	10.49	0.03
14	1629.85	56.01	0.12	1645.28	1620.21	6.3	0.01
15	1739.79	56.24	1.31	1801.51	1699.29	24.97	0.5
16	2951.09	54.85	0.77	2987.74	2914.44	18.9	0.22
17	3211.48	54.44	0.05	3215.34	3197.98	4.58	0
18	3340.71	54.38	0.09	3344.57	3305.99	10.12	0.02
19	3458.37	55.14	0.06	3464.15	3452.58	2.99	0
20	3535.52	56.25	0.4	3572.17	3525.88	11.41	0.08

Comment; BFO Date/Time; 6/23/2017 2:57:27 PM No. of Scans; Resolution;
User; Administrator

Figure 2.7 FTIR Diagram of pure BFO

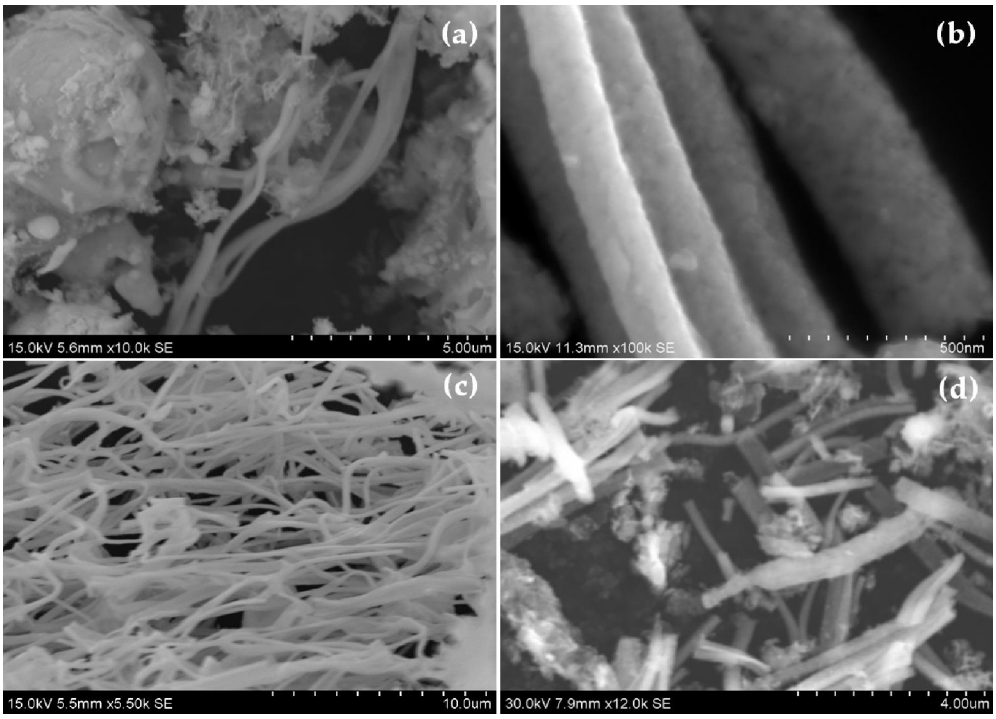

Figure 2.8 SEM Diagram of Pure BFO

(a) 8 kv it 's not sufficient Small diameter.
(b) 10 kv large diameter, Poor mechanical strength.
(c) 15 kv excellent fiber, homogenous Size distribution, diameter of size 50-100 nm
(d) 20 kv very small length, were fibers are broken relatively in homogenous.

2.14 X-Ray diffraction result:

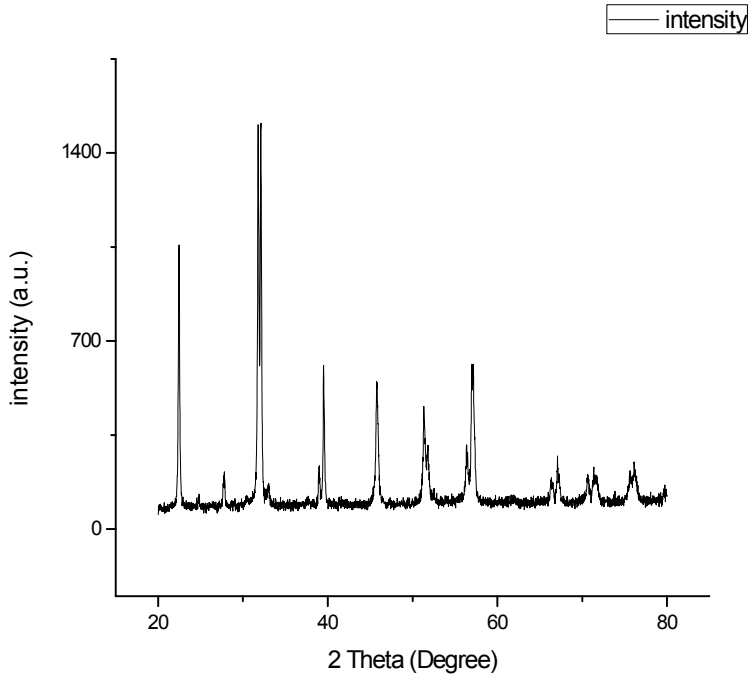

Figure 2.9 Powder x-ray diffractogram for BFO

Calculation of Particle size:

Particle size= 0.89λ/β cos θ

Here λ=1.54A°, β=FWHM,

Then particle size=0.9*1.54A°/ β*0.0174*cos θ, So

FWHM=x2-x1, >33-32=1A °, FWHM=0.1nm, then and 2θ=31.6059, θ=15.80, then cos θ=0.9622

And Particle size =(0.89*1.54)/(1*0.962)=14.24nm.

INTERPLANAR SPACING

nλ=2dsinθ n=1,2…, Here n=1

Sin (11.245)	d=4.05 A°
Sin (13.968)	d=3.19A°
Sin (15.8807)	d=2.8143 A°
Sin (19.7053)	d=2.28A°
Sin (23.0098)	d=1.97A°
Sin (25.8007)	d=1.77 A°
Sin (28.6694)	d=1.605 A°
Sin (33.5952)	d=1.39A°

Table 2.1

XRD measurements were performed to characterize the crystal structure of the calcined powders. As shown in Figure 2.5, all the XRD patterns can be indexed to pure rhombohedral perovskite structure, which are in good agreement with the powder of pure BFO sample.

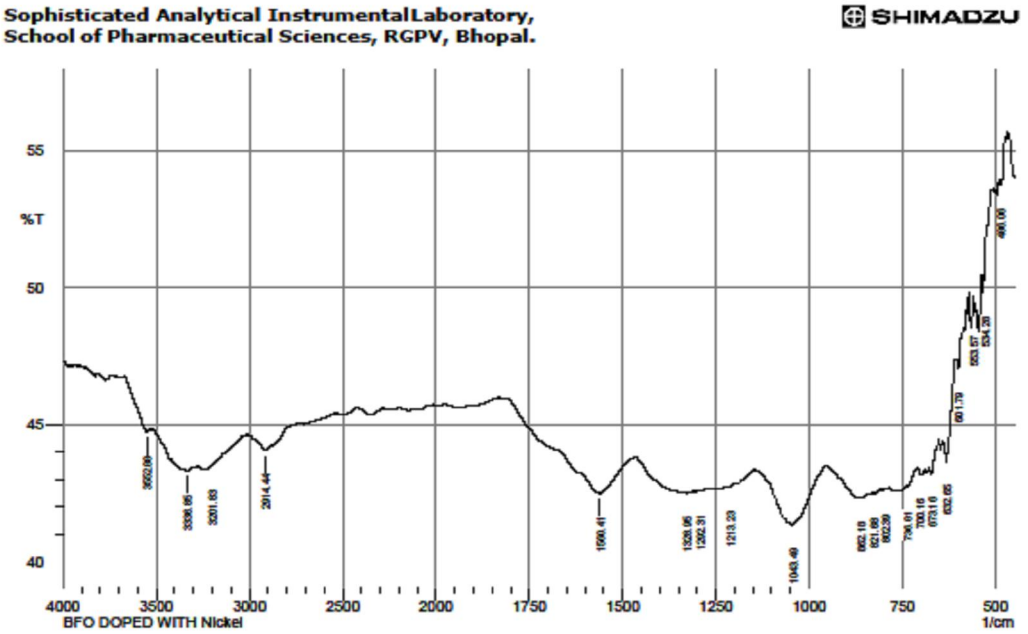

No.	Peak	Intensity	Corr. Intensity	Base (H)	Base (L)	Area	Corr. Area
1	486.06	53.76	0.56	489.92	474.49	4.1	0.06
2	534.28	49.81	0.81	536.21	511.14	7.09	0.02
3	553.57	49.09	0.21	559.36	551.64	2.37	0.01
4	601.79	47.06	0.44	603.72	586.36	5.57	0.02
5	632.65	43.66	1.1	636.51	609.51	9.3	0.18
6	673.16	43.2	0.38	677.01	653.87	8.31	0.05
7	700.16	43.14	0.22	709.8	690.52	7.02	0.02
8	736.81	42.72	0.09	738.74	711.73	9.89	0.02
9	802.39	42.61	0.05	808.17	786.96	7.85	0.01
10	821.68	42.46	0.1	829.39	810.1	7.16	0.01
11	862.18	42.32	0.05	867.97	844.82	8.63	0.01
12	1043.49	41.34	2.09	1143.79	954.76	70.47	1.99
13	1213.23	42.72	0.02	1215.15	1145.72	25.45	0.03
14	1292.31	42.58	0.01	1294.24	1271.09	8.57	0
15	1328.95	42.5	0.02	1332.81	1307.74	9.31	0
16	1560.41	42.49	0.98	1614.42	1477.47	50.19	0.72
17	2914.44	44.06	0.27	2974.23	2881.65	32.79	0.12
18	3201.83	43.47	0.04	3205.69	3159.4	16.67	0
19	3336.85	43.31	0.07	3346.5	3311.78	12.6	0.02
20	3552.88	44.75	0.1	3570.24	3543.23	9.41	0.01

Comment;

BFO DOPED WITH Nickel

Figure 2.9 FTIR Diagram of BFO Doped with Nickel

After heat treatment at 350◦C, the sample from nitric acid precursor begins to generate pure phase BFO while another sample from sodium hydraoxide acid precursor is still of amorphous feature. It is clear that the crystallization of BFO completed at a temperature of 350◦C for nitric acid precursor while 450◦C for sodium hydraoxide acid precursor, which is used to reduce the effect of nitric acid. Meanwhile, the particle size of BFO changed remarkably after further heat treatment.

Calcined at temperatures above 550◦C, well-crystallized and pure phase BFO can be obtained for either precursor. As discussed in early literatures, the grain sizes of BFO NPs grow up with increasing the temperature in soft chemical routes [21, 26]. This can be also confirmed by the peak sharpening of XRD curves.

FTIR Results for Nickel doped BFO:

The above figure gives the information of compression and expansion of particle after doping of Nickel in BFO, with the help by establish the reltionship between frequency and wave number.

Shows the room temperature UV–visible diffuse reflectance spectra of Bi1-xNixFeO3 samples. It seems that pristine BFO nano particles exhibit two absorption peaks at 475nm and 585nm, which shift to a lower wavelength in case of doped samples. As a semiconductor, it is well-known that the optical absorption properties of BFO are related to the electronic structure and play the key role in determining their bandgaps. The energybandgaps (Eg) of samples were calculated by classical Tauc formula. In this case, the absorptioncoefficient α (here α¼4πk/λ) and the photon energy hν for directly allowed transitions are related as: (ahν)2¼A (hν_Eg), where A is a constant function. The Eg values are therefore determined by extra polating the linear portion of the plot relating (αhν)2 versus hν to (ahν)2¼0.

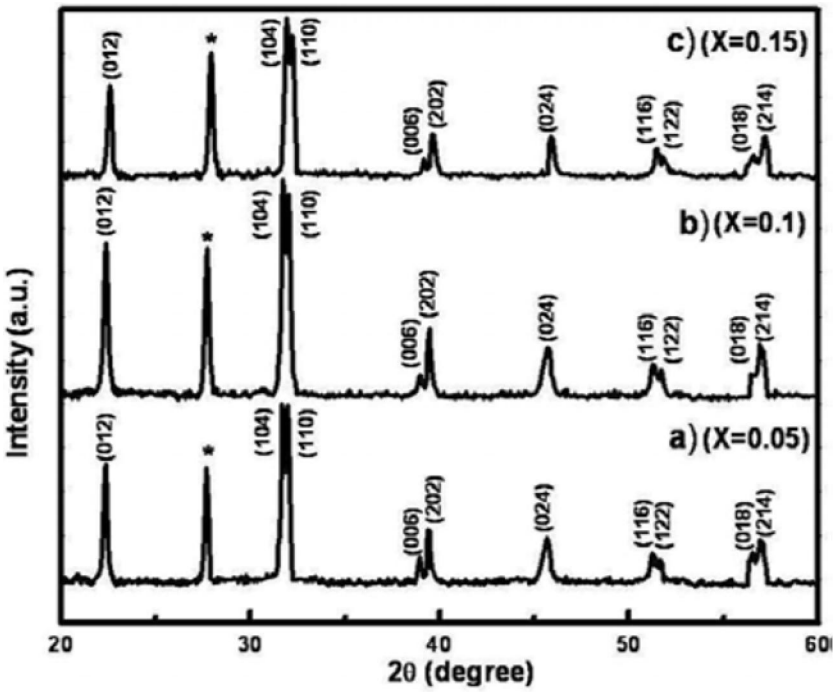

Figure 2.10 XRD Diagram of BFO Doped with Nickel

Figure 2.11 demonstrates the room-temperature X-ray diffraction (XRD) patterns of BiFe0.95Ni0.05O3, BiFe0.9Ni0.1O3 and BiFe0.85Ni0.15O3 ceramics. The XRD patterns depict that, BiFe1-*x*Ni*x*O3 samples crystallize in a rhombhohedral perovskite phase in the doping range of $0.05 \leq x \leq 0.15$. Moreover, an additional impurity phase corresponding to Bi12NiO19 has been spotted around 30° in the 2θ range. Typically, it is very difficult to prepare a single-phase BiFeO3, as the product is frequently contaminated with some secondary phases like Bi2O3, Bi2Fe4O9 and Bi12(Bi0.5Fe0.5) O19.5 [21,25]. The XRD results are in well accord with the reported results by Wang *et al*. [23]

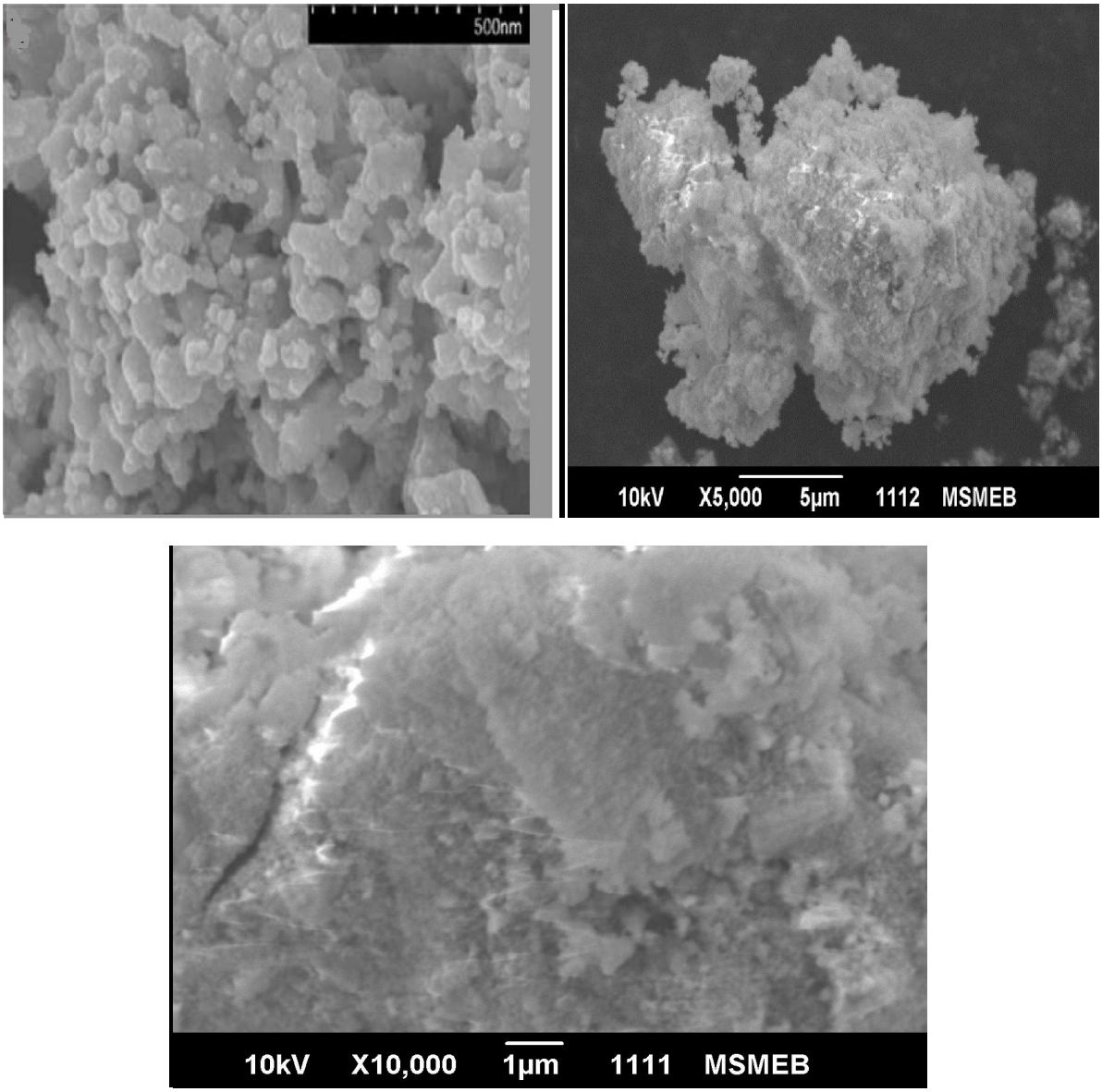

Figure 2.11 SEM Diagram of BFO Doped with Nickel

SEM:

The field emission scanning electron microscope (FESEM) is used to observe the morphological details of the sample. Figure 3 shows the images of the BFO sample for both undoped and 5mol% Ni-doped after annealing at 500 °C in air for 10-12 hr at higher and lower resolutions.

For both pure BFO and Ni-doped sample, anisotropic growth with few interconnected pores among the agglomerated particulates is noted. Agglomerates have irregular polygonal to bimodal shape structures. Both samples exhibit strong agglomeration tendency among the granular particulates. Particle size for the undoped perovskite bismuth ferrite is about 20 nm while that for Ni-doped sample is found to be about 22 nm.

EDX: The EDX results clearly confirm the presence of essential elements for the successful synthesis of the BFO-based material. Presence of Ni peak exhibits doping effect on the bismuth ferrite matrix which validates with corresponding experimental findings from X-ray diffractogram study with shift in the peak towards left.

XRD measurements were performed to characterize the crystal structure of the calcined powders. As shown in Figure 2.9, all the XRD patterns can be indexed to pure rhombohedral perovskite structure. After heat treatment at 550◦C, the sample from citric acid precursor begins to generate pure phase BFO while another sample from 350◦C is still of amorphous feature. It is clear that the crystallization of BFO completed at a temperature of 550◦C for citric acid precursor while 350◦C, which is in good line with the analysis. Meanwhile, the particle size of BFO changed remarkably after further heat treatment. Calcined at temperatures above 450◦C, well-crystallized and pure phase BFO can be obtained for either precursor. As discussed in early literatures, the grain sizes of BFO NPs grow up with increasing the temperature in soft chemical routes [21, 26]. This can be also confirmed by the peak sharpening of XRD curves. [41]

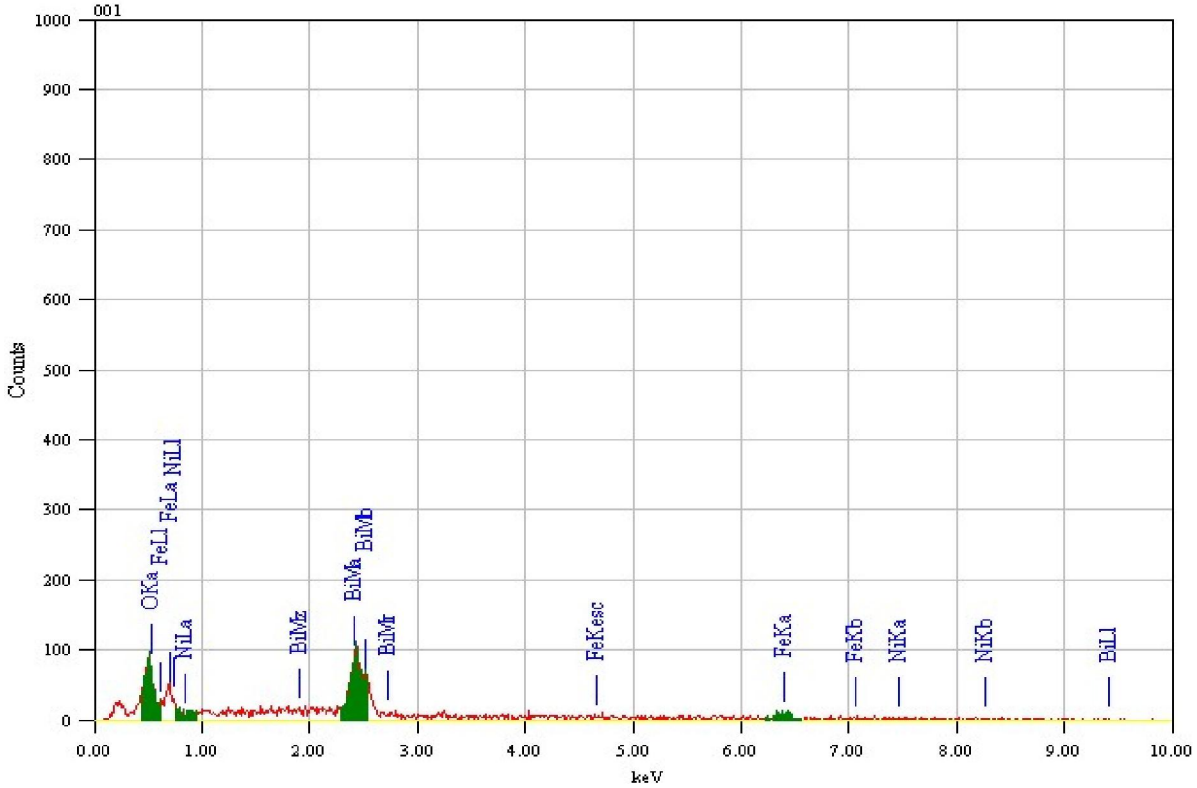

Figure 2.12 EDX Diagram of BFO Doped with Nickel

The morphology of the calcined BFO nanoparticles was examined by SEM. Typical SEM images are shown in Figure 2.8. It is clear that the spherical NPs formed from both are sufficiently fine and uniform and the particle sizes are about 14nm, respectively.

Our NPs are well crystallized, and both can be indexed to pure BFO rhombohedral crystal structure. The XRD image of individual BFO NP clearly shows an interplanar spacing of 1.39 A° to, 4A°. We can expect the size of NPs with an average particle size of about 14 nm through keeping the calcinations temperatures at 450, 550 respectively. Figure 2.8 shows the FTIR spectra of BiFeO3 precursors using tartaric acid and citric acid as chelating, respectively. As shown, eight characteristic IR peaks appeared for BFO precursor, while four characteristic IR peaks together with some weak peaks appeared for BFO precursor using citric acid as chelating. Both samples have two sharp and one wide IR peaks, which correspond to the stretching vibrations of C=O and –OH. The IR wide peaks located at 3866 cm−1 were assigned to the stretching vibrations of structural hydroxyl (OH) groups, and the intense peaks at 1648–1696 cm−1 were assigned to the stretching vibrations of C=O. The IR peaks located at 1421cm−1 were attributed to the symmetry bending vibration of C–H. In addition, a sharp IR peak located at 1293cm−1 was assigned to the stretching vibration of single bond of C–O for tartaric acid precursor sample, while it cannot

be observed for citric acid precursor sample. The IR peaks below 1000 cm−1 (such as 512, 836, and 942cm−1 for tartaric acid precursor, 617, 591, 683, 898, and 990 cm−1 for citric acid precursor) were corresponding to the vibrations bonds of Bi–O or Fe–O, respectively. Firstly, Bi (NO3)3·5H2O and Fe (NO3)3·9H2O along with chelating agents were added to the deionized water and formed the complex of Bi and Fe. Secondly, sol-like precursor and irregular particles come into being followed by aqueous solution were dried. [42]

Phase analysis of Figure of shows the X-ray diffraction of Ni-doped BFO heat treated at 550 °C for 1. Diffraction peak corresponding to maximum intensity 10-12 hr sintering required to seen at particle which matches with the pure phase of bismuth ferrites [17]. The average crystallite size was estimated by Scherrer's formula t = 0.9_/(_ cos _B) (where t is crystallite size, _ is half width full maxima, _B is angle between_1 and _2) from XRD data shown in Table2.1. The crystallite size increases with increasing calcined temperature due to thermally activated diffusion. [39]

Ni-doped BFO powders calcined at 550 °C exhibits a small amount of secondary Bi2Fe4O9 phase, whereas XRD patterns of the samples heat treated at 550 and 600 °C have a few week peaks of the secondary phase. Thus, in subsequent experiments, annealing temperature was maintained at 500 °C to obtain the desired phase purity. The 3mol% Ni-doped BFO annealed at 550 °C shows very weak peaks of the secondary Bi2Fe4O9 phase. When concentration of dopant increases to the extent of 5 and 10mol%, peaks of Bi2Fe4O9 phase remain similar which are shown in Fig. 2.1. However, the crystallite size for the sample with 5mol% doping is found to be smaller than 3 and 10mol% doping. The crystallite sizes of all samples are given in Table 1. The secondary phase does not induce any constraints to the properties of nanocrystallite BFO as it can be seen from the subsequent observations. It was also shown that it is difficult to remove the secondary phase even by strong concentrated nitric acid leaching.

Figure 2.10 shows the small shifting of the strongest XRD peak due to the doping of BFO with Ni. The crystallite size of 5mol% Ni doped bismuth ferrite is about 15.4 nm compared to the undoped perovskite bismuth ferrite which is about 14.7 nm. Atomic radius of Ni2+ (0.72Å) is comparable with Fe3+ (0.64Å) which may be the possible reason for doping of B site of ABO3 perovskite (bismuth ferrite) with transitional metal ion. Due to the slight variation atomic radius, strain will be generated in the matrix which may be the cause for slight reduction of crystallite size in Ni-doped sample 3.2. Microstructural and elemental analysis The synthesized powder is spread over a conducting carbon tape, and a field emission scanning electron microscope (FESEM) is used to observe the morphological details of the sample. Figure 3 shows the images of the BFO sample for both undoped and 5mol% Ni-doped after annealing at 500 °C in air for 30 minutes at higher and lower resolutions. For both undoped and Ni-doped sample, anisotropic growth with few interconnected pores among the agglomerated particulates is noted. Agglomerates have irregular polygonal to bimodal shape structures. Both samples exhibit strong agglomeration tendency among the granular particulates. Particle size for the undoped perovskite bismuth ferrite is about 20 nm while that for Ni-doped sample is found to be about 22 nm. The above results are closely connected to the experimental findings from our crystallite size measurement from XRD studies using Scherrer's formula. Hence, we confirmed that synthesis of the nanocrystalline undoped and Nidoped bismuth ferrite with perovskite structure was performed successfully.

Conclusions:

Chemical route can be used to synthesize nanocrystalline undoped and Ni-doped bismuth ferrite with perovskite structure and crystallite size of about 14nm and 15.4 nm, respectively. Rise in doping concentration leads to generation of secondary phase, thus dopant concentration is maintained to 5mol%. Morphological analyses exhibits irregular polygonal to bimodal shape agglomerates with few interconnected pores. Dielectric constant for the undoped bismuth ferrite is about 100, while for 5mol% Ni doped sample it is noted around 600 (at low frequency). Such drastic change leads to higher polarizability which also enhances ferroelectricity with Ni doping on perovskite bismuth ferrite. Both nanocrystalline and Ni-doped BFO exhibits super paramagnetic nature due to suppression of spin cycloid magcycloid magnetic moment. Saturation magnetization of Ni-doped is slightly lower than for undoped BFO due to smaller crystallite size.

Authors:
Dr Jyotsna Chauhan*, Poonam Patel
*HOD Department of Nanotechnology, Rajiv Ganhi Techanical University, Bhopal (M.P.), India
*Corresponding authors
E-mail- jyotsnachauhan2006@gmail.com

References:

1. Drexler, K. Eric (1986). Engines of Creation: The Coming Era of Nanotechnology. Doubleday. *ISBN 0-385-19973-2*.

2. Jump up^ Apply nanotech to up industrial, agri output, *The Daily Star* (Bangladesh), 17 April 2012.
3. Chaudhari YA, Singh A, Abuassaj EM, *et al*. Multiferroic properties in BiFe1 *x*Zn*x*O3 (*x* = 0.1–0.2) ceramics by solution combustion method (SCM).
4. Qin W, Guo YP, Guo B, *et al*. Dielectric and opticalproperties of BiFeO3–(Na0.5Bi0.5) TiO3 thin films deposited on Si substrate using LaNiO3 as buffer layer for photovoltaic devices. *J Alloys Compd* 2012.
5. S. Li, Y.-H. Lin, B.-P. Zhang, C.-W. Nan, and Y. Wang, "Photocatalytic and magnetic behaviors observed in nanostructured BiFeO3 particles," *Journal of Applied Physics*, vol. 105, no. 5, Article ID 056105, 2009.
6. T.-J. Park, G. C. Papaefthymiou, A. J. Viescas, A. R. Mooden baugh, and S. S. Wong, "Size-dependent magnetic properties of single-crystalline multiferroic BiFeO3 nanoparticles," W. Eerenstein, N. D. Mathur, and J. F. Scott, "Multiferroic and magnetoelectric materials," *Nature*, vol. 442, no. 7104, pp.759–765, 2006.
7. P. Fischer, M. Polomska, I. Sosnowska, and M. Szymanski, "Temperature dependence of the crystal and magnetic structures of BiFeO3," *Journal of Physics C*, vol. 13, no. 10, pp. 1931–1940, 1980.
8. C. Tabares-Munoz, J. P. Rivera, A. Monnier, and H. Schmid,"Measurement of the quadratic magnetoelectric effect on single crystalline BiFeO3," *Japanese Journal of Applied Physics*, vol. 24, pp. 1051–1053, 1985.
9. Y. P. Wang, L. Zhou, M. F. Zhang, X. Y. Chen, J.-M. Liu, and Z. G. Liu, "Room-temperature saturated ferroelectric polarization in BiFeO3 ceramics synthesized by rapid liquid phase sintering," *Applied Physics Letters*, vol. 84, no. 10, pp. 1731–1733, 2004.
10. M. Fiebig, T. H. Lottermoser, D. Fr¨ohlich, A. V. Goltsev, and R. V. Pisarev, "Observation of coupled magnetic and electric.
11. I. E. Dzyaloshinskii, Sov. Phys. JETP 10, 628 (1960).
12. D. N. Astrov, Sov. Phys. JETP11, 708(1960).
13. V. J. Folen et al., Phys. Rev. Lett. 6, 607(1961).
14. Hans Schmid, Ferroelectrics162, 317-338 (1994).
15. Daniel Khomskii Physics 2, 20 (2009).
16. A. M. Glazer, Acta Cryst. B28, 3384 (1972).
17. J. A. Bartkowska, International Journal of Thermophysics 32, 739 (2011).
18. Smolensky GA, Isupov VA, Agronovskaya AI, Sov Phys Solid State 1, 150 (1959).
19. Achenbach GD, James WJ, Gerson R, Am J. Ceram Soc. 50, 437 (1967).
20. Kubel F, Schmid H. Acta Crystallogr B 46, 698 (1990).
21. Spaldin, K. M. Rabe, M. Wuttig and R. Ramesh, Science 299, 1719 (2003).
22. A. K. Zvezdin, and D. Viehland, Appl. Phys. Lett. 84, 5261 _ (2004).
23. C. Ederer and N. A. Spaldin, Phys. Rev. B 71, 224103 (2005).
24. Ederer C, Spaldin NA. Phys Rev. B 71, 224103 (2005).
25. Mei Z. G, Shang S, Wang Y, Liu Z-K. Apply Phys. Lett. 98, 131904 (2011).
26. G. Catalan and J. F. Scott, Advanced Materials, 21, 2463 (2009).
27. A. G. Gavriliuk et al., Phase transition with suppression of magnetism in BiFeO3 at high pressure. Condensed Matter 4, Volume 82, 224 (2005).
28. a) Palemicz A. et al., Act Cryst. B 63: 537 (2007).
29. b) Palemicz A. et al., Acta Phys. Pol. A 117, 296 (2010).
30. Scott JF. J Magn Magn. D. J. Norris, (1995). "Measurement and Assignment of the Size-Dependent Optical Spectrum in Cadmium Selenide (CdSe) Quantum Dots, MIT". *hdl:1721.1/11129 (1995).*
31. "Nanotechnology Information Center: Properties, Applications, Research, and Safety Guidelines". American Elements (1998).
32. M. Cahay (2001). Quantum Confinement VI: Nanostructured Materials and Devices: Proceedings of the International Symposium. The Electrochemical Society. ISBN 978-1-56677-352-2. Retrieved 19 June 2012.
33. H. Haug; Stephan W. Koch (1994). Quantum Theory of the Optical and Electronic Properties of Semiconductors. World Scientific. ISBN 978-981-02-2002-0. Retrieved 19 June 2012.
34. T. V. Lippen, R. No¨tzel, G. J. Hamhuis, and J. H. Wolter, J. Appl. Phys. 97, 044301 (2005).
35. R. G. Nuzzoand D. L. Allara, J. Am. Chem. Soc.105,4481 (1983).
36. M. Giersigand P. Mulvaney, Langmuir 9,3408(1993).
37. S. Chaure, N. B. Chaure, and R. K. Pandey, J. Nanosci. Nanotechnol.
38. 7,945(2007).
39. J. Mazher, S. Badwe, R. Sengar, D. Gupta, and R. K. Pandey.
40. Physica E 16, 209 (2003).
41. S. Chaure, N. B. Chaure, and R. K. Pandey, J. Nanosci. Nanotechnol.
42. Journal of Applied physics 98(4).
43. P. M. Aneesh et al. (2007) " synthesis of ZnO nanoparticles by hydrothermal method"

nanophotonic material IV, Proc. Of SPIE Vol. 6639, 66390J.
44. S Ilican, Caglar Y., Caglar M., (2008), Preparation and characterization of ZnO thin films deposited by sol-gel spin coating method. Journal of optoelectronics and advanced materials. 10:2578–2583.
45. L. E. Brus. Electron-electron and Electron – hole interaction in small semiconductor crystallites: The size dependence of the lowest exited electronic state. Journal of Chemistry Physics. 80. 9. 1984.
46. Y. Wang, A. Suna, W. Mahler, and R. Kasowski, J. Chem. Phys.87, 7315 (1987).
47. . LW. Wangand A. Zunger, Phys. Rev. B.51,17398(1995).
48. P. E. Lippensand M. Lannoo, Phys. Rev. B.39,10935(1989).
49. L. E. Brus, J. Che. Phys.80,4403(1984).
50. N. A. Hilland K. B. Whaley, J. Chem. Phys.100,2831(1994).
51. S. Sapraand D. D. Sharma, Phys. Rev. B.69, 125304(2004).
52. H. Fuand A. Zunger, Phys. Rev. B.55, 1642(1997).

5/23/2018